remote sensing

MDPI

Article

Fusion of Sentinel-2 and Sentinel-3 Images for Producing Daily Maps of Advected Aerosols at Urban Scale

Luciano Alparone [1,*], Massimo Bianchini [2], Andrea Garzelli [3] and Simone Lolli [4]

[1] Department of Information Engineering, University of Florence, 50139 Florence, Italy
[2] IFAC-CNR, Consiglio Nazionale delle Ricerche, 50019 Sesto Fiorentino, Italy; massimo-bianchini@cnr.it
[3] Department of Information Engineering and Mathematics, University of Siena, 53100 Siena, Italy; andrea.garzelli@unisi.it
[4] CNR-IMAA, Consiglio Nazionale delle Ricerche, 85050 Potenza, Italy; simone.lolli@cnr.it
* Correspondence: luciano.alparone@unifi.it

Highlights

What are the main findings?
- Calculate dense maps of Aerosol Optical Depth (AOD) from Sentinel-2/3 images.
- Discriminate the type of AOD, either coarse or fine, from its scattering properties.

What are the implication of the main findings?
- The maps produced from S2 and S3 data are merged to achieve a spatio-temporal fusion.
- The method does not require the availability of ground-based auxiliary data.

Abstract

In this study, the authors wish to introduce an unsupervised procedure designed for real-time generation of maps depicting advected aerosols, specifically focusing on desert dust and smoke originating from biomass combustion. This innovative approach leverages the high-resolution capabilities provided by Sentinel-2 imagery, operating at a 10 m scale, which is particularly advantageous for urban settings. Concurrently, it takes advantage of the near-daily revisit frequency afforded by Sentinel-3. The methodology involves generating aerosol maps at a 10 m resolution using bands 2, 3, 4, and 5 of Sentinel-2, available in L1C and L2A formats, conducted every five days, contingent upon the absence of cloud cover. Subsequently, this map is enhanced every two days through spatial modulation, utilizing a similar map derived from the visible and near-infrared observations (VNIR) captured by the OLCI instrument aboard Sentinel-3, which is accessible at a 300 m scale. Data from the two satellites undergo independent processing, with integration at the feature level. This process combines Sentinel-3 and Sentinel-2 maps to update aerosol concentrations in each 300 m × 300 m grid every two days or more frequently. For the dates when Sentinel-2 data is unavailable, the spatial texture or the aerosol distribution within these grid cells is extrapolated. This spatial index represents an advancement over prior studies that focused on differentiating between dust and smoke based on their scattering and absorption characteristics. The entire process is rigorously validated by comparing it with point measurements of fine- and coarse-mode Aerosol Optical Depth (AOD) obtained from AERONET stations situated at the test sites, ensuring the reliability and accuracy of the generated maps.

Keywords: AERONET; aerosols; atmospheric absorption; atmospheric scattering; data fusion; Sentinel-2; Sentinel-3

Academic Editors: Disong Fu, Kai Wu, Hongrong Shi and Yu Zheng

Received: 3 November 2025
Revised: 19 December 2025
Accepted: 23 December 2025
Published: 29 December 2025

https://doi.org/10.3390/rs18010116

1. Introduction

Aerosols consist of minute particles suspended in the atmosphere that arise from both natural events and human endeavors. These particles, although short-lived, possess a wide array of characteristics and effects, making them a focal point in various scientific fields. Recent research [1] underscores the key role that the chemical components of atmospheric aerosols play in shaping public health and climate conditions. This influence manifests itself through mechanisms such as the scattering and absorption of light (direct effects) and alterations in the dynamics and persistence of clouds (indirect effects), which influence air quality in the boundary layer [2,3]. Further investigation [4] delves into the complex impact of aerosols on precipitation patterns, revealing that they can enhance or suppress rainfall depending on their concentration and function as cloud condensation nuclei. A recent study [5] investigates the relations between dust outbreaks and heat waves on the Iberian Peninsula. Another study highlights the importance of understanding how aerosols drive climate change [6], to inform the formulation of effective environmental policies, as elaborated in their sustainability research. Moreover, aerosols significantly affect the incoming energy of the Sun by modulating the interaction with solar radiation. They can decrease the efficiency of solar panels by scattering and absorbing sunlight, thus decreasing the incoming solar radiation.

The study of various types of aerosols, particularly the identification of biomass burning events and dust outbreaks using multispectral imaging (MSI), is a key aspect of remote sensing (RS) research, especially in the Mediterranean basin. This area is uniquely vulnerable due to its distinct geographical and climatic characteristics, which make it prone to recurrent dust storms emanating from the Sahara Desert [7], as well as biomass burning advections. These phenomena have profound consequences on air quality, climatic conditions, and human health. Interestingly, the Mediterranean is recognized as a “climate hotspot,” a designation that underscores the accelerated pace of climate change in this region compared to other areas [8–10]. In the past ten years, the Sentinel satellite series, which forms an integral part of the European Space Agency’s (ESA) Copernicus program, has played an indispensable role in monitoring these environmental events. The advanced capabilities of MSI on these satellites have been instrumental in providing invaluable data for this purpose. Their ability to capture detailed MSI facilitates comprehensive analysis and a greater understanding of the atmospheric dynamics at play, thereby significantly contributing to the field of environmental science and public health policy.

The combustion of biomass, which includes phenomena such as wildfires and agricultural burns predominantly initiated by landowners according to the findings in [11], contributes to the substantial emission of aerosols and trace gases into the troposphere, which affects the quality of air and climatic conditions. Aerosols generated from smoke have the ability to spread over large distances from their point of origin. The Sentinel-2 satellite, equipped with its high-resolution Multispectral Instrument (MSI), plays a key role in the detection and surveillance of such occurrences. Sentinel-2’s integration of visible, near-infrared, and short-wave infrared (SWIR) spectral bands facilitates the discrimination of burned regions from their adjacent landscapes by leveraging the distinct reflectance characteristics of charred vegetation versus unburned soil. As elucidated in [12], we underscored the Sentinel-2 multi-wavelength imaging capability to identify intense aerosol emissions from combusting biomass, through the incorporation of polarized data, which significantly improves detection precision [12]. In addition, advances in algorithms tailored for Sentinel-2 datasets have expedited the detection and mapping of burned zones, enabling near instantaneous surveillance of biomass combustion episodes. The use of techniques based on machine learning and deep learning has shown significant potential in increasing the accuracy and efficacy of detecting and categorizing burned territories [13].

https://doi.org/10.3390/rs18010116

Focusing our examination on another significant atmospheric issue, we encounter the challenge posed by dust emissions, predominantly originating from the Sahara Desert, which presents unique complexities in the realm of aerosol monitoring [14–16]. These dust events exert a substantial influence on air quality, modulating sunlight exposure, and affecting ecosystem dynamics [7,17–19]. The Sentinel-3 satellite, equipped with advanced instruments such as the Ocean and Land Color Instrument (OLCI) and the Sea and Land Surface Temperature Radiometer (SLSTR), plays a pivotal role in acquiring critical data necessary for the identification and surveillance of dust occurrences. Sentinel-3 mass spectroscopy capabilities facilitate the detection of dust plumes using specific combinations of spectral bands, notably the Dust Index (DI) and the Normalized Difference DI (NDDI). These indices capitalize on the unique spectral characteristics of atmospheric dust [20].

Subsequent research efforts employ an integrated approach that involves multiple RS techniques. This includes leveraging data from operational Lidar and solar photometer networks in conjunction with Sentinel datasets to analyze Saharan dust and aerosols from biomass burning in the Mediterranean Basin [21] and during the aftermath of Hurricane Ophelia [22]. This underscores the synergistic advantages that arise from the combination of satellite [23] and ground-based observational methods for effective aerosol monitoring. In a similar vein, the study presented in [24] demonstrates the efficacy of using a composite approach involving ceilometers, sun photometers, and the MultiSpectral Instrument (MSI) for the detection and characterization of dust and smoke phenomena. Furthermore, Lidar technology has the ability to discriminate between different types of aerosol within urban landscapes [25]. Despite these advances, significant challenges persist [26], more specifically within urban environments, where achieving detailed resolution is crucial to effective street-level aerosol-detection.

This study presents a method for the detection, evaluation, and monitoring of aerosols in urban environments over time by creating an AOD index from Sentinel-2 images, similar to that recently proposed by some of the authors [15]. The limited temporal repetition of Sentinel-2 is mitigated by spatiotemporally merging the 10 m maps produced from four Sentinel-2 bands with the 300 m maps produced from the same number of corresponding bands of the Sentinel-3 OLCI instrument, available with a temporal repetition of less than two days. The procedure is validated through correlations with point measurements of AOD in fine/coarse mode performed by AERONET stations available at the test sites.

The structure of the article is described below. Section 2 and its subsections describe the instruments used: Sentinel-2 MSI, Sentinel-3 OLCI, and the AERONET network of ground stations; then the index, calculated from the two types of Sentinel data, and the spatial fusion procedure used to combine the related maps. Experimental results on two datasets are presented and discussed in Section 3. Some conclusions and possible developments are the subject of Section 4.

2. Materials and Methods

2.1. Sentinel-2 MSI

The Sentinel-2A and 2B satellites form a twin constellation that provides multispectral imaging (MSI) in the visible, near-infrared (VNIR), and short-wave infrared (SWIR) regions, achieving global coverage with a five-day revisit time [27]. These satellites are equipped with 13 spectral bands, as depicted in Figure 1. Among these, the VNIR bands B2, B3, B4 and B8 offer the finest spatial resolution, with a ground sampling distance (GSD) of 10 m. Bands B5, B6, and B7 in the red-edge (RE) region, the narrow NIR band B8a (centered at 865 nm), and SWIR bands B11 and B12 are delivered at an intermediate resolution of 20 m GSD. The remaining lower-resolution bands—B1, B9, and B10—have a GSD of 60 m and are primarily intended for atmospheric applications, including the retrieval of ozone, coastal aerosols, water vapor, and cloud ice, rather than for direct Earth observation. These variations in spatial resolution arise from intrinsic trade-offs of spatial detail, spectral discrimination, and radiometric sensitivity in electro-optical instruments. Multispectral band sharpening is commonly applied to enhance spatial resolution when higher-detail images are required. The approaches followed are based on component substitution and multi-resolution analysis [28]. Thus, one can increase the resolution of the bands taken at 20 m and 60 m, using the four bands at 10 m and then apply a multi-platform fusion [29].

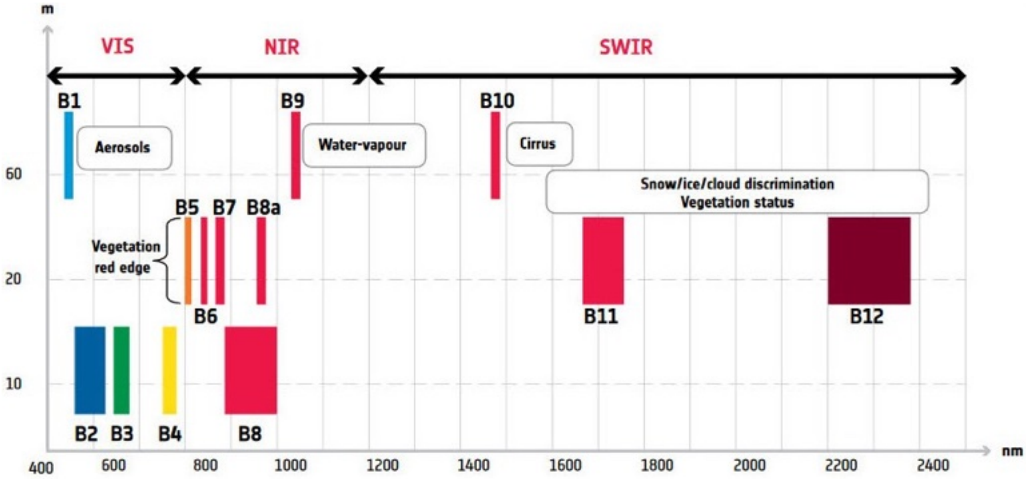

Figure 1. Architectural design of Sentinel-2 spectral bands. B1 is optimized for aerosol measurement; B5–B7 and B8a to observe vegetation dynamics, including the red edge phenomenon; B6 and B8 for comprehensive vegetation analysis; B9 to assess water vapor content; B10 for identifying cirrus clouds; B11, B12 for distinguishing among snow, ice, and clouds, and conducting advanced assessments of vegetation health. These bands span wavelengths from 400 nm to 2400 nm. Bandwidths are visually represented by the lengths of colored bars. The vertical scale represents the spatial resolution (m).

Optical data collected through RS technologies are predominantly distributed in formats such as spectral radiance and reflectance. Spectral radiance is characterized as the radiance rescaled according to the spectral span of the instrument. Reflectance is quantified within the range [0, 1] and is categorized into two distinct types: top-of-atmosphere (TOA) reflectance and bottom-of-atmosphere (BOA) reflectance, also known as surface reflectance when measured at sea level [30]. The TOA reflectance is essentially the surface spectrum as it is perceived through the atmospheric layers by the satellite, and it is computed by rescaling the TOA spectral radiance with the TOA spectral irradiance of the Sun. Conversely, BOA reflectance encapsulates the Earth surface spectral signature, necessitating the estimation of both the upward and downward atmospheric transmission coefficients and the upward scattered radiance at TOA. These estimates can be achieved through parametric modeling or direct empirical measurements [31]. Furthermore, TOA spectral radiance is recognized as a level 1 (L1) product, whereas the TOA reflectance, referred to as the L1C product, is typically accessible for systems that perform nadir acquisition and offer comprehensive global Earth coverage. Examples of such systems include Landsat 7 Enhanced Thematic Mapper Plus (ETM+), Landsat 8–9 Operational Land Imager (OLI), and Sentinel-2 A/B. Additionally, surface reflectance is classified as a level two product (L2A) and is likewise distributed for systems providing global Earth coverage. Sentinel-2 products, specifically at L1C and L2A levels, are readily available for free access through online platforms, thus facilitating extensive research and applications in RS.

2.2. Sentinel-3 OLCI

Sentinel-3 serves as a complement to Sentinel-2 with its moderate resolution capabilities. Each satellite in this constellation is equipped with a pair of instruments. The Ocean and Land Colour Instrument (OLCI) covers the VNIR range through 21 narrow bands at a spatial resolution of 300 m, targeting specific absorption events. Figure 2 illustrates the arrangement of the OLCI spectral bands. Notably, NIR bands are broader than VIS bands, due to NIR radiation being ineffective for ocean color analysis because it is minimally reflected by water. Sentinel-3A and Sentinel-3B were launched on 16 February 2016 and 25 April 2018, respectively.

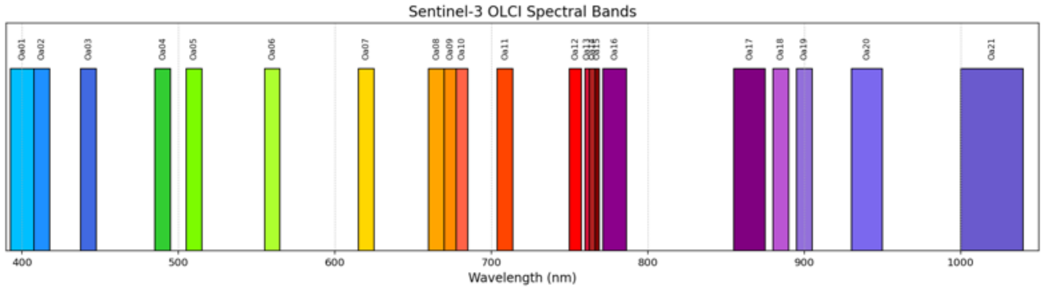

Figure 2. Sentinel-3 OLCI layout of spectral bands. Wavelengths span from 390 nm to 1050 nm, with differing widths and intervals. Band widths range in (2.5, 3.75, 7.5, 10, 15, 20, 40) nm.

The Ocean and Land Colour Instrument (OLCI) was designed to extend the data continuity of the Medium Resolution Imaging Spectrometer (MERIS) from the EnviSat mission. OLCI is a visible spectrum pushbroom radiometer comprising five camera modules that capture data across 21 spectral bands, spanning wavelengths from 400 nm to 1200 nm. These cameras are fan-configured vertically, orthogonal to the spacecraft's trajectory, with each camera covering a 14.2° field of view and a 0.6° overlap with adjacent cameras. The entire field is tilted 12.6° off-track to reduce Sun glint interference. Calibration is ensured via onboard Sun diffuser hardware.

The L1C OLCI dataset is generated from packed spectral radiance and associated metadata. TOA reflectance is calculated by adjusting for exoatmospheric solar irradiance, by multiplication to the cosine of the solar zenith angle. OLCI may lack L2A surface reflectance data; however, surface reflectance, which is more temporally stable than atmospheric parameters, can be deduced from the downsampled L2A product of Sentinel-2 from a nearby date when Sentinel-2 data is accessible.

2.3. AERONET

The Aerosol Robotic Network, abbreviated as AERONET [32], is an extensive global network of uniform ground-based Sun photometers. The network was launched as part of the Earth Observation Program by the National Aeronautics and Space Administration (NASA). It has been strategically installed in various global locations. The operational oversight of both permanent and temporary observation sites is undertaken by a combination of academic institutions and governmental agencies. The Sun photometers, which are the product of Cimel Electronique, have been indispensable in the comprehensive assessment of both aerosol and cloud characteristics. This is largely attributed to the robustness and longevity of the measurements facilitated by AERONET. The data obtained are of paramount importance for integration with satellite observations, thus improving the scientific understanding of the environmental and climatic impacts of aerosols. The AERONET database, which is freely accessible to the public at https://aeronet.gsfc.nasa.gov/, (accessed on 20 October 2025), is extensively utilized by numerous researchers, governmental bodies, and various stakeholders worldwide. Its purpose is to support policy formulation and augment scientific knowledge concerning Earth's systems. The effectiveness of the network is primarily derived from the standardized nature of the instruments, measurement protocols, and data analysis methodologies employed. This standardization is crucial to ensure that the resulting data and subsequent analysis are reliable and consistent.

The Aerosol Robotic Network (AERONET) employs a network of ground-based sun photometers to perform spectral measurements of aerosol optical depth (AOD) across various wavelengths. This technique facilitates the extraction of fine- and coarse-mode optical depths specifically at the reference wavelength of 500 nm utilizing the aerosol spectral deconvolution algorithm (SDA). This approach differentiates the optical thickness of the cloud, categorized as the element of the coarse-mode, from the optical depth of the fine-mode aerosol (AOD) as referenced in [33]. This distinction is made possible even when clouds and aerosol are intermixed. By employing this method, one can thoroughly examine how clouds contribute to the amplification of the fine-mode AOD. The analysis provides insight into the interactions between clouds and aerosols, highlighting their influence on enhancing fine-mode aerosol optical properties, which is crucial for assessing the impact of clouds on fine-mode AOD when both elements coexist. Extensive research using AERONET data has revealed significant variations in fine-mode AOD enhancements that are seasonal and regional. These variations are attributed to multiple factors, including the hygroscopic growth of aerosol particles and processes that occur within clouds, leading to marked discrepancies in fine-mode AOD enhancements in diverse global regions [34]. Such studies underscore the complexity of atmospheric phenomena and highlight the importance of understanding cloud-aerosol interactions in different climatic and geographical contexts.

In recent times, academic efforts have progressively addressed the detailed characterization of aerosol size distributions with the subsequent implications these have on the processes involved in retrieving aerosol optical depth (AOD) measurements. The necessity of integrating both fine and coarse aerosol modes into analytical models has been emphasized, as these are crucial to understanding aerosol dynamics and their possible climate impacts [35]. In this regard, we employ data from version 3 level 1.5 [36]. The aerosol products that separate fine and coarse modes are essential for evaluating occurrences such as dust storms and biomass burning in specific geographic areas. The applied retrieval method performs a comprehensive spectral breakdown of the AOD data, allowing us to distinguish between the effects of fine particles, which are generally smaller and often associated with human activities or secondary natural aerosols, and coarse particles, which are typically larger and mainly originate from primary natural sources such as mineral dust and sea salt. This ability to distinguish is crucial for accurately identifying the type of aerosol in a specific location.

2.4. Aerosol Spatial Index

Based on the analysis of TOA reflectance spectra [15], we formulate the Dust/Biomass Burning Index (DBB) at (i, j) to distinguish smoke from dust aerosols in the multispectral images of Sentinel-2. This index is characterized by: (a) its differential nature, as it considers the response difference between aerosol events and clear skies on two dates, functioning as a calibration; (b) its normalized attribute, ensuring insensitivity to the surface reflectance of the scene's; (c) its composition property, achieved by averaging wavelength specificity into a cumulative index. In this research, the band selections have been modified to match the spectral overlap between the Sentinel-2 MSI and Sentinel-3 OLCI bands, as detailed in Figures 1 and 2. The newly chosen bands are (B2, B3, B4, B5) for Sentinel-2 and (Oa04, Oa06, Oa08, Oa11) for OLCI, excluding SWIR bands since OLCI lacks them. The modified index, namely DBB-2, is defined for both instruments accordingly.

$$\text{DBB-2}(i,j) = \frac{1}{4}\sum_{k} \frac{\rho_k^{(\text{TOA})}(i,j) - \overline{\rho}_k^{(\text{TOA})}(i,j)}{\overline{\rho}_k^{(\text{BOA})}(i,j)} \quad k = 2,3,4,5\ (\text{S2}),\ \ k = 4,6,8,11\ (\text{OLCI}) \tag{1}$$

in which $\rho_k^{(\text{TOA})}$ represents the TOA reflectance for the test image in the kth band, obtained from the L1C Sentinel-2 A/B product (see Figure 1) or the L1C Sentinel-3 A/B OLCI product (see Figure 2). The term $\overline{\rho}_k^{(\text{TOA})}$ denotes the TOA reflectance of a reference capture of the same instrument at the same location, under clear atmospheric conditions, specifically where the combined AOD of the coarse and fine aerosol modes is at least below 0.07. The normalization term in Equation (1), $\overline{\rho}_k^{(\text{BOA})}$, is the kth band of L2A surface reflectance product of the reference clear image. The index in Equation (1) is computed at the pixel level to produce aerosol maps at 10 m (the 20 m band B5 is preliminarily interpolated by two). Since the surface reflectance product L2A is not available for OLCI, it has been replaced by a downsampled version of that of Sentinel-2. This is feasible because the surface reflectance is slowly varying because it does not depend on rapidly varying atmospheric conditions.

The spatial distributions of the suggested index offer a comprehensive overview of the type and concentration of aerosols, specifically: (1) Saharan dust, which is highly reflective, thus increasing the value of the index in Equation (1) (DBB-2 > 0); (2) biomass burning aerosol (BBA) absorbs radiation rather than scattering it, leading to decreased TOA reflectance at identical wavelengths and resulting in a negative index (DBB-2 < 0). Under clear atmospheric conditions, DBB-2 values typically approach zero.

To derive a unique aerosol index similar to AERONET station data, the suggested pixel index should be averaged across the scene, preferably excluding water pixels. This is due to the instability of the normalization term in Equation (1) over water, which has variable reflectance spectra over time as water color changes with the sky [15]. Enhanced differentiation between dust and smoke aerosols is achievable by averaging across areas without water pixels, when feasible. Identification of water pixels is possible by thresholding the surface reflectance of B12, with the Sentinel-2 L2A product indicating $\rho_{B12} < 1\%$, as recommended by ESA (see https://step.esa.int/thirdparties/sen2cor/2.10.0/docs/S2-PDGS-MPC-L2A-ATBD-V2.10.0.pdf, (accessed on 20 October 2025) and https://sentiwiki.copernicus.eu/web/s2-mission, (accessed on 20 October 2025).

2.5. Data Fusion

Extensive studies on RS image fusion for Earth Observation have been conducted over several decades, leading to numerous fusion techniques. Image fusion can be categorized by sensor homogeneity. Homogeneous fusion involves images from identical imaging mechanisms, termed *unimodal* fusion, with MS pansharpening (the combination of multispectral and panchromatic data) being the most prevalent. This involves combining data reflecting solar radiation at varying wavelengths and spatial resolutions. In contrast, *multimodal* fusion integrates data sets from different imaging modes.

Fusion methods can be differentiated according to the content level they address: (i) pixel level, (ii) feature level, and (iii) decision level [28]. At the pixel level, fusion combines image pixel values to create a fused image, predicting missing spatial details of multispectral (MS) data using a panchromatic (Pan) image and an injection model, possibly accounting for the atmosphere [37]. Feature-level fusion involves merging separately extracted image descriptors. For optical and SAR image fusion, direct pixel combination is discouraged to prevent speckle contamination [38], and instead uses texture or change features [39]. Decision-level fusion consolidates classification maps from different data sets or classifiers, resulting in a comprehensive classification map.

For spatio-temporal fusion, a feature-based approach is ideal. Here, the 10 m resolution AOD map from Sentinel-2 is fused with the near-daily 300 m resolution AOD map from Sentinel-3. The fusion rule involves modulating the Sentinel-2 AOD map, normalized over a 300 × 300 m^2 window, with the resampled 10 m Sentinel-3 AOD map:

$$\text{DBB-2}^{F}(i,j) = \frac{\text{DBB-2}^{(S2)}(i,j) \cdot \text{DBB-2}^{(S3)} \uparrow 30(i,j)}{(\text{DBB-2}^{(S2)} \downarrow 30) \uparrow 30(i,j)} \quad (2)$$

in which $\text{DBB-2}^{F}(i,j)$ indicates the temporally fused spatial map, achieved from the individual maps obtained from Sentinel-2 and Sentinel-3, respectively, $\downarrow r$ denotes decimation by r, $\uparrow r$ interpolation by r, $r = 300/10$ is the scale ratio between S3-OLCI and S2-MSI. Decimation employs a boxcar filter; interpolation is achieved using "à trous" filters [40]. This choice satisfies the consistency requirements, temporal and spatial [41] in the present case. The flow chart of the fusion scheme appears in Figure 3.

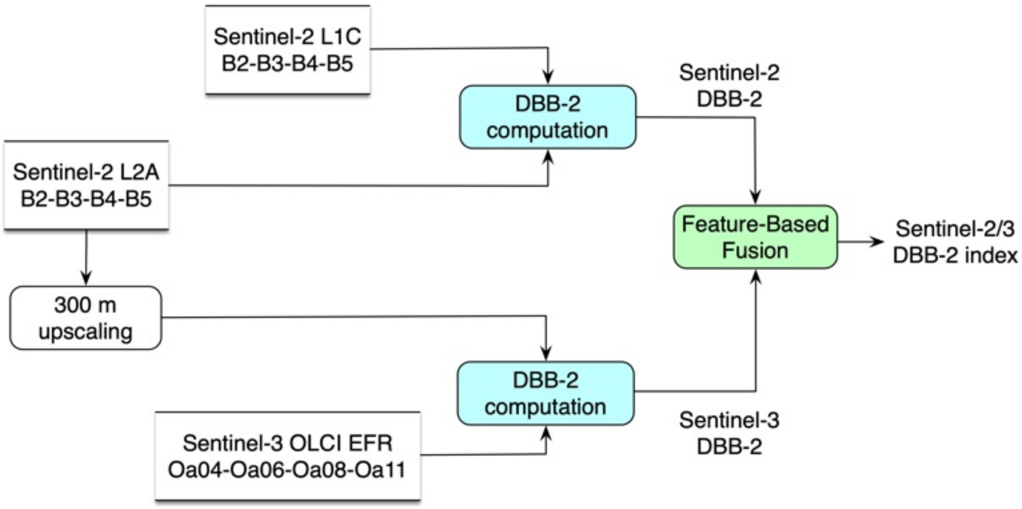

Figure 3. Block diagram for calculation of the multiplatform aerosol index. Input data products are: S2 L1C (Top-Of-Atmosphere reflectance) @ 10 m; S2 L2A (Bottom-Of-Atmosphere reflectance) @ 10 m; S3 L1C @ 300 m. S3 L2A data products are not available and are obtained by upscaling S2-L2A products before applying Equation (1). The feature-based fusion rule is described in Equation (2). In the absence of cloud cover, the S2 DBB-2 map is available every five days; the S3 DBB-2 map every two days, same as the fused map, S2/3 DBB-2.

3. Results

3.1. Dust Outbreak Event

The initial test site, located in the industrial hub of Tito Scalo near Potenza in the southern region of Italy, was impacted by a substantial Saharan dust phenomenon by late March 2024 [42]. Figure 4 presents the Sentinel-2 MultiSpectral Instrument (MSI) data acquisitions, including both L1-C and L2-A data products, recorded on 01 April 2024 at 09:59:31 (S2A), which is one day after the event's peak, and on 05 June 2024 at 09:59:35 (S2B), a day noted for clear atmospheric conditions serving as a reference. The presence of aerosols is clearly observable in the Top of Atmosphere (TOA) reflectance data represented in Figure 4a. In contrast, Figure 4b predominantly demonstrates Rayleigh scattering associated with atmospheric constituents. The surface reflectance measurements illustrated in Figure 4c,d exhibit a striking resemblance, with shadow effects due to variations in solar elevation over the two-month period being compensated by using Shuttle Radar Topography Mission (SRTM) digital elevation models at a 30 m resolution. The AERONET sun photometer is strategically placed within the premises of the Institute of Environmental Analysis Methodology (CNR-IMAA) of the National Research Council at coordinates 40.60°N, 15.72°E, which is indicated by a red circle in Figure 4d. Situated about 2 km southeast of the AERONET site is a minor lake. The significance of water bodies is underscored by their surface reflectance variability in response to atmospheric sky conditions [15]. For the derivation of Aerosol Optical Depth (AOD) maps from Sentinel-2 imagery, water pixels can be effectively masked by applying thresholds to certain Visible Near-InfraRed (VNIR) or Short-Wave InfraRed (SWIR) spectral bands. However, in the context of Sentinel-3 imagery, water pixels might be dispersed over a broader area, rendering them unmaskable without altering the intrinsic geometry of the water bodies. In the ensuing discussion of this section, water pixels undergo no distinct processing, as is typically done with MODIS aerosol products.

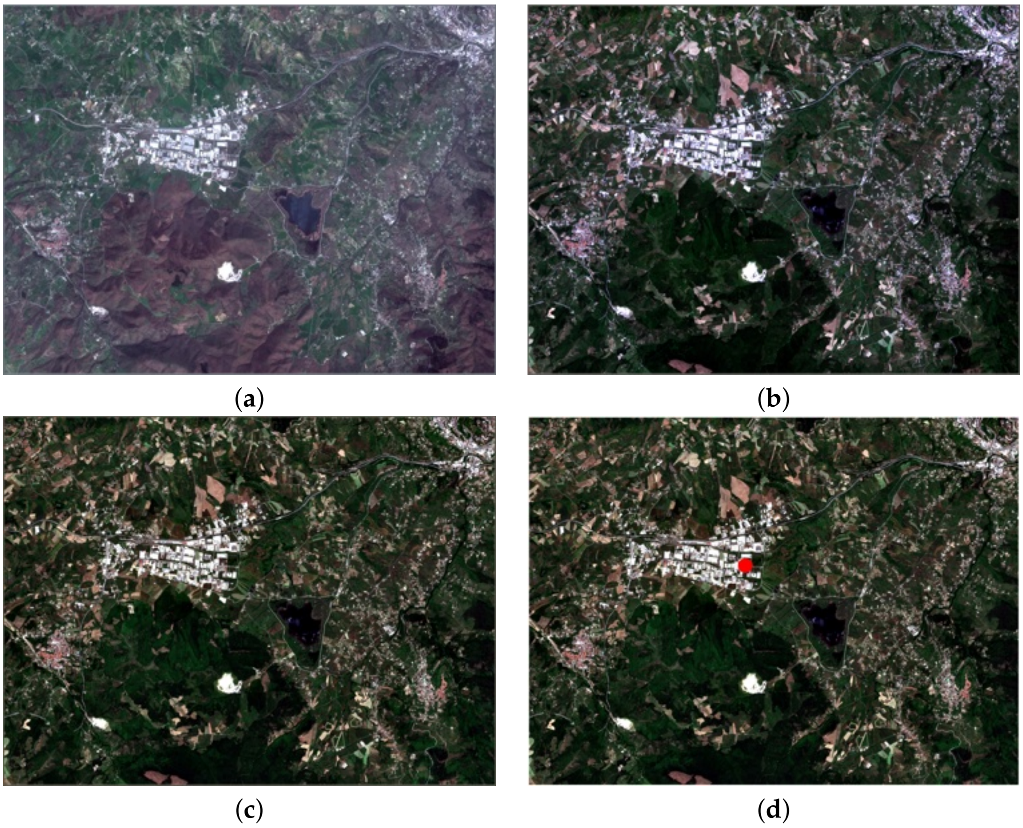
(**a**) (**b**) (**c**) (**d**)

Figure 4. True color composition (B4, B3, B2) of 9 × 12 km^2 B4-B3-B2 of Sentinel-2. Top-Of-Atmosphere reflectance: (**a**) 01 April 2024; (**b**) 05 June 2024. Bottom-Of-Atmosphere reflectance: (**c**) 01 April 2024; (**d**) 05 June 2024 (red dot marks position of AERONET station).

Figure 5 illustrates Sentinel-3's OLCI Earth Observation Full Resolution (EFR) for the following dates and times: 30 March 2024 at 08:46:25 UTC (S3A) on the event's peak day, 01 April 2024 at 09:32:02 UTC (S3A) as the event declined, 07 April 2024 at 09:37:56 UTC (S3B) during the event absence, and 05 June 2024 at 09:11:12 UTC (S3B) on a clear reference day. The limited spatial resolution makes it challenging to distinguish whether Figures 4b and 5b capture identical scenes in the same instance and in the same spectral bands.

Figure 6 shows the DBB-2 maps for peak, middle, and vanishing events. The consistent radiometry between fused and unfused maps is immediately noticeable. Urban areas with stable surface reflectance over the two months between events and clear days are effectively eliminated in both high-resolution and fused maps. Subtle texture variations, potentially stemming from uncorrected shadow, may manifest as AOD fluctuations. The high-resolution S2 data is only available on the mid-event day, while the peak and event conclusion are traceable through fused maps. The test site did not show significant spatial changes in the aerosol distribution. In particular, unlike nonnegative AOD, the DBB-2 index can be negative, particularly in smoke conditions [15], where absorption supersedes scattering, reducing total scattered radiation below clear sky levels.

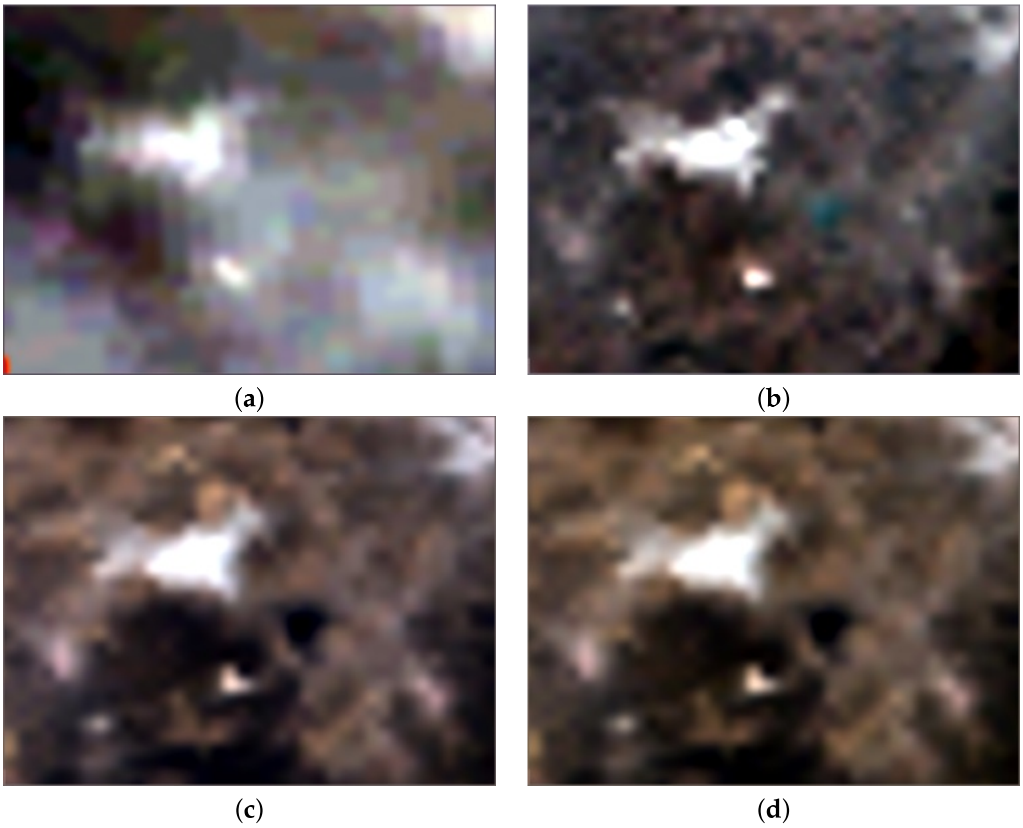
(**a**) (**b**)
(**c**) (**d**)

Figure 5. Same 9 × 12 km^2 scene as in Figure 4 with a compositions of bands 8, 6, 4 (R-G-B true color) of OLCI Top-Of-Atmosphere reflectance acquired on: (**a**) 30 March 2024; (**b**) 01 April 2024; (**c**) 07 April 2024; (**d**) 05 June 2024.

Despite the limitations of the proposed index on water pixels [15], the small water basin near the Tito Scalo urban area is included to demonstrate the spatial precision of the 10 m Sentinel-2 data. The reduced accuracy of fused maps, caused by mixed pixels of the OLCI, is insignificant since water bodies typically undergo masking before applying the index in Equation (1).

Cross-referencing with the total AOD SDA from the AERONET station is presented in Table 1. The total AOD of AERONET SDA is measured at the red dot in Figure 4. DBB-2 values represent the average of the maps, excluding water pixels, as S2 and S3 observe the Earth's surface nadir, thus measuring a vertical atmospheric column. AERONET, however, observes off-zenith, resulting in a nonvertical atmospheric column corrected for the solar zenith angle, covering a larger test area. The DBB-2 and AERONET measurement discrepancies, especially at peak events, may stem from water vapor presence, adjustable using OLCI's L2 water vapor column product, akin to AERONET's method. The alignment between DBB-2 and AERONET AOD suggests that the index in Equation (1) is theoretically sound, despite the challenges in mitigating surface texture from space imaging.

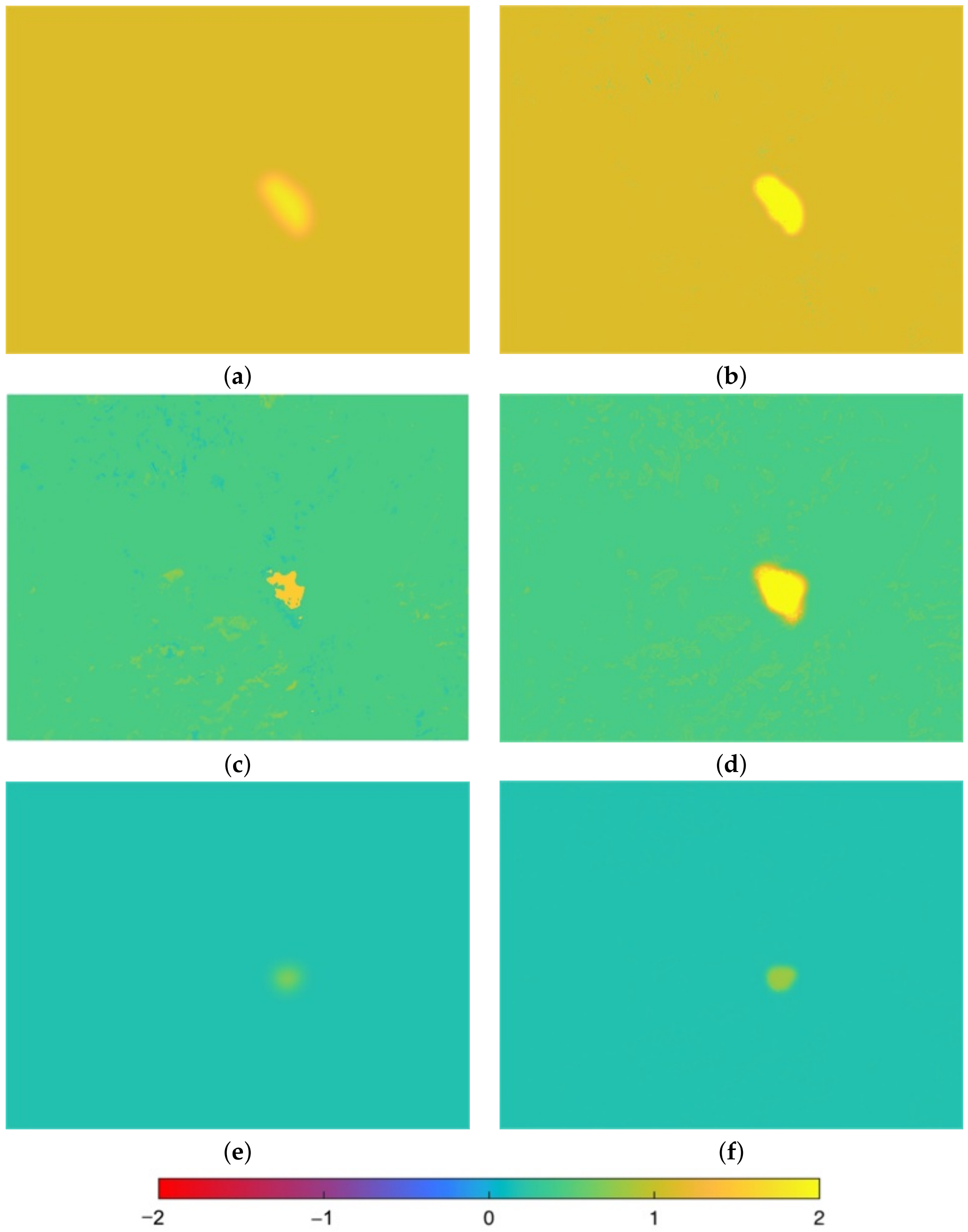

Figure 6. DBB-2 maps following the evolution of the dust outbreak: (**a**) OLCI on 30/03; (**b**) OLCI + S2 on 30/03; (**c**) S2 on 01/04; (**d**) OLCI + S2 on 01/04; (**e**) OLCI on 01/07; (**f**) OLCI + S2 on 01/07.

Table 1. AERONET Total SDA AOD (Coarse + Fine) compared to the values proposed by DBB-2, derived either from Sentinel-2 or from the integration of maps generated from S2 and S3-OLCI. On the clear day of 5 June 2024, DBB-2 is defined as zero. An AOD level below 0.07 signifies a clear day. AERONET AOD measurements are taken at the red dot shown in Figure 4, while DBB-2 values are the average of the respective maps, with water pixels excluded.

	AERONET AOD	**DBB-2 (S2)**	**DBB-2 (OLCI + S2)**	**DBB-2 (OLCI)**
30 March 2024	1.01	-	1.111	1.110
1 April 2024	0.40	0.408	0.406	0.404
7 April 2024	0.07	-	0.083	0.083
5 June 2024	0.05	0	0	0

3.2. Biomass Burning Event

An alternative testing location is proposed in the Barcelona metropolitan region of Spain, featuring an AERONET station at coordinates 41.39°N, 2.11°E, located at an altitude of 125 m. We have collected Sentinel-2 images from a 72 km^2 region that includes urban, vegetated, and industrial areas. The clear-sky reference acquisition was taken on 2 April 2023. The true-color TOA reflectance (L1C) is shown in Figure 7b; true-color BOA reflectance (L2A) in Figure 7d. The identical region was downloaded for testing purposes, with an acquisition on 24 October 2020 related to a biomass burning event. Figure 7a illustrates the true-color images in L1C, while Figure 7c presents them in L2A. The presence of smoke increases the bluish component, due to Rayleigh scattering, and makes the image somewhat darker, due to the absorption of the aerosols.

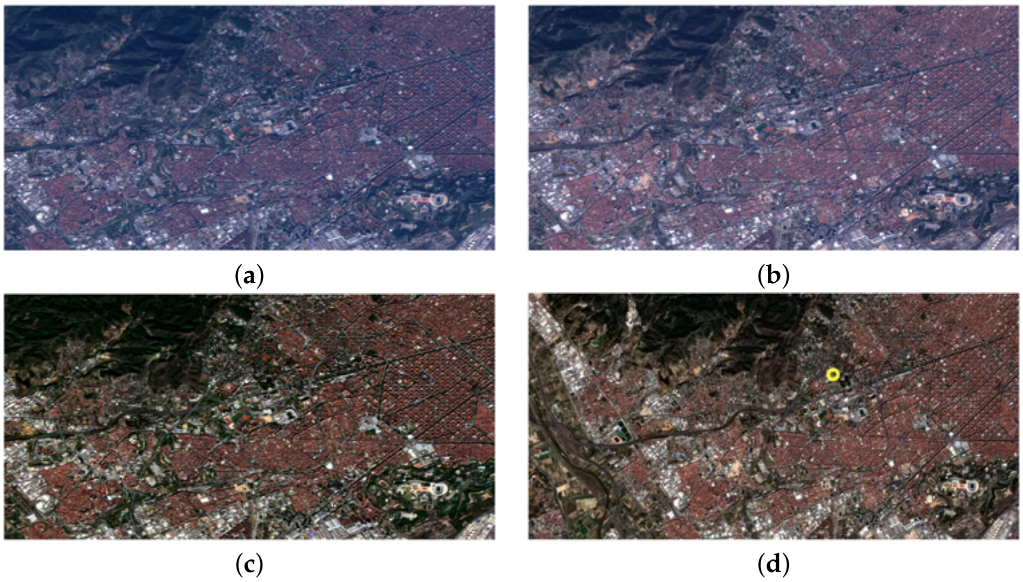

Figure 7. True color composition (B4, B3, B2) of 6 × 12 km^2 B4-B3-B2 of Sentinel-2 over the city of Barcelona. Top-Of-Atmosphere reflectance: (**a**) 24/10/2020; (**b**) 02/04/2023. Bottom-Of-Atmosphere reflectance: (**c**) 24/10/2020; (**d**) 02/04/2023 (yellow dot marks position of AERONET station).

Figure 8 shows the Sentinel-3 Ocean and Land Color Instrument (OLCI) Earth Observation Full Resolution (EFR) true-color compositions: 24/10/2020 at 10:09:23 UTC (S3A) (biomass burning event); 28/10/2024 at 10:05:39 UTC (S3A) (decreasing event); 02/04/2023 at 10:09:28 UTC (S3A) (clear day). Figure 8d shows the BOA reference image with 300 m resolution obtained from the Sentinel-2 L2A image by upscaling from 10 m to 300 m.

Figure 9 displays the spatial maps of DBB-2, in the four cases: peak of the event, only S2 and S2 merged with S3 (OLCI); end of the event, four days later, only S3 and S3 merged with S2 taken four days earlier. A first consideration is that the values of DBB-2 are negative, as expected, because smoke absorption further reduces Rayleigh scattering. The sign of DBB-2 allows coarse (dust) and fine (smoke) aerosols to be discriminated, unlike Sentinel-2 AOD products, in which the extinction of radiation is measured, but not brought back to the nature of particles.

Eventually, a cross-reference with AERONET's measures is reported in Table 2. The match is strong on the date of the peak of the event; weaker on the date of the end of the event. The overestimation can be blamed on the greater amount of water vapor. In fact, the modulus of DBB-2 is always biased in excess. Note that the modulus of DBB-2 indicates the AOD; the sign indicates the dominant type of aerosol dust or smoke.

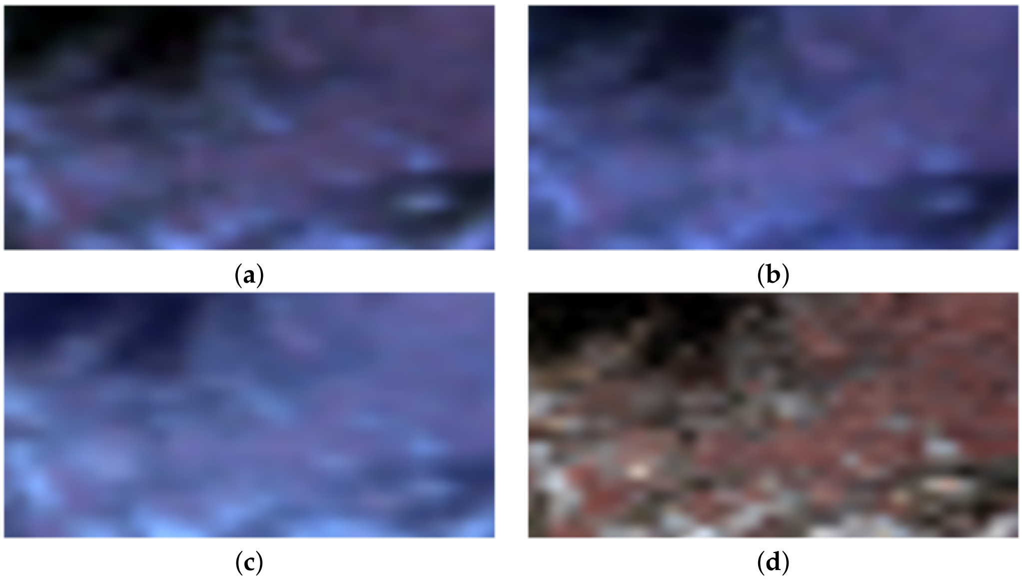

Figure 8. Same 6 × 12 km^2 scene as in Figure 7 with a compositions of bands 8, 6, 4 (R-G-B true color) of OLCI Top-Of-Atmosphere reflectance acquired on: (**a**) 24 October 2020; (**b**) 28 October 2020; (**c**) 02 April 2023. The BOA reflectance of the reference, clear-sky image at 300 m resolution is shown in (**d**).

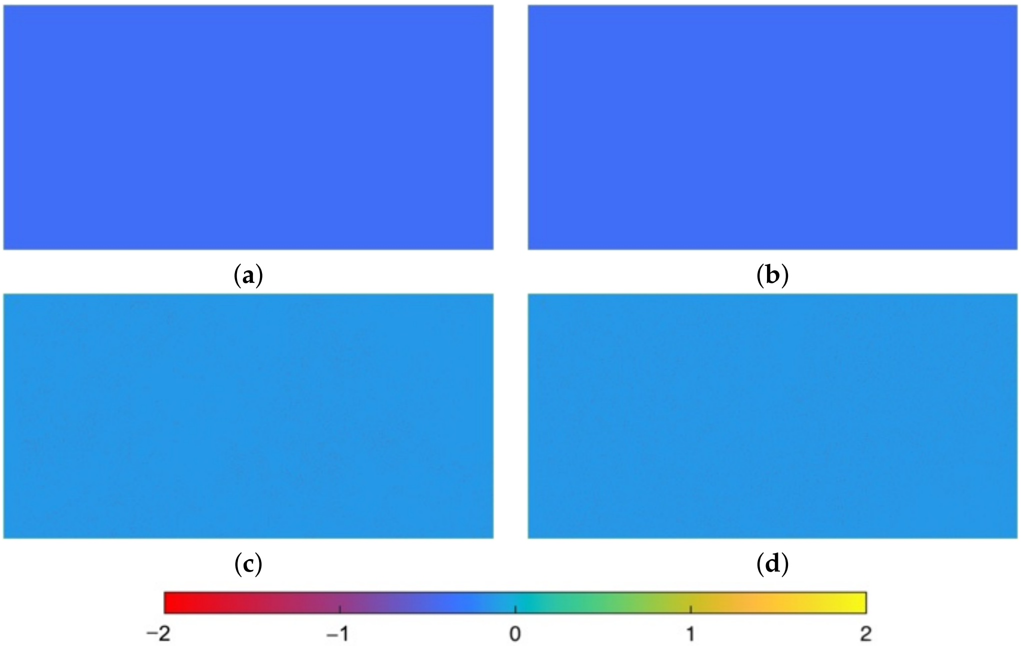

Figure 9. DBB-2 maps following the evolution of the burning event: (**a**) S2 on 24 October 2020; (**b**) OLCI + S2 on 24 October 2020; (**c**) OLCI on 28 October 2020; (**d**) OLCI + S2 on 28 October 2020.

Table 2. Comparison of AERONET Total SDA AOD (at 500 nm) and values of DBB-2, either calculated from S2 or from the fusion of maps calculated from S2 with maps calculated from S3-OLCI. On the clear day (02-04-2023), DBB-2 is zero by definition. AOD below 0.07 indicates that the day is clear. AERONET AOD is measured on the yellow circle in Figure 7; DBB-2 values are average of the respective maps.

	AERONET AOD	DBB-2 (S2)	DBB-2 (OLCI + S2)	DBB-2 (OLCI)
24 October 2020	0.089	−0.092	−0.091	−0.092
28 October 2020	0.053	-	−0.060	−0.060
2 April 2023	0.029	0	0	0

3.3. Discussion

The spatial index defined in Equation (1) tends to mimic the process by which AERONET estimates the coarse and fine AODs, with the problem that the measurement is no longer point-specific, but rather extended over areas. Furthermore, the AERONET measurement depends on the solar radiation incident on the ground. The satellite measurement relates to the round trip of incident solar radiation through the atmosphere reflected by the ground. This explains why the spectral signature of the ground, that is, the surface reflectance, is eliminated by the normalization term in Equation (1). We wish to recall that DBB-2 is not a physical measurement of AOD, because it may also be negative. It may be interpreted as the difference between coarse mode AOD and fine mode AOD. Therefore, DBB-2 attains positive or negative values depending on the dominating type of aerosol. If there is only one type of aerosol, DBB-2 is expected to be more accurate.

AERONET distinguishes between fine aerosols and coarse aerosols using the spectral deconvolution algorithm (SDA), based on AODs measured in various bands and Ångström exponent. However, validating such fine–coarse partitioning would require a dense and reliable network of ground-based instruments (e.g., sunphotometers and/or Lidars), which is not currently available. Furthermore, satellite-derived AOD products from systems such as Sentinel-2, Sentinel-3, and MODIS do not provide the necessary information to discriminate among different aerosol types. Therefore, satellite AOD maps alone cannot be used to validate or reproduce the fine–coarse aerosol separation obtained from AERONET.

The clear day is crucial, because the contribution to radiation extinction due to molecular scattering (Rayleigh scattering) must be separated from that of aerosols. There is an additional contribution that depends on water vapor. Rayleigh scattering is calculated analytically by AERONET, since the main atmospheric constituents have practically constant concentrations, the contribution of water vapor is always calculated analytically, after measuring the water vapor content in the band around 940 nm. Therefore, while Equation (1) eliminates Rayleigh scattering, it leaves the contribution of water vapor. Figure 10 shows the average TOA reflectance spectra of the scene in Figure 7a,b, plus another spectrum of an apparently clear day, i.e., without aerosols, but with a certain amount of vapor, which still contributes to haze formation. The presence of water vapor on the clear day conceals the presence of moderate amounts of smoke in the test scene and overestimates the amount of dust, whereas the presence of vapor in the test scene underestimates the amount of dust.

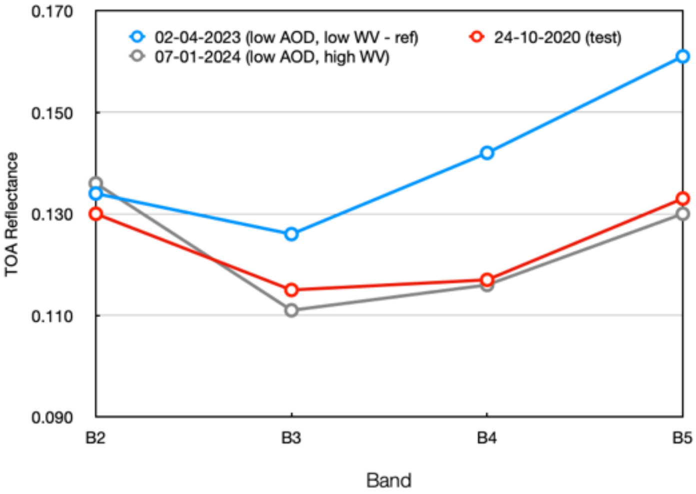

Figure 10. Average Top-Of-Atmosphere Sentinel-2 reflectance spectra: the presence of water vapor in the 07-01-2024 observation makes the clear day indistinguishable from the smoky day. Instead, in the observation of 02-04-2023, the spectrum of the clear day is far apart from that of the smoky day.

The improper selection of clear-day reference conditions can affect the baseline TOA reflectance spectra used for aerosol index calculations, potentially reducing the sensitivity to certain aerosol types. However, the magnitude of this effect differs significantly among aerosol species due to their distinct optical properties. Desert dust exhibits high single scattering albedo values (0.94–0.98 at visible wavelengths), indicating strong scattering with minimal absorption due to low imaginary refractive indices. In contrast, biomass burning smoke shows substantially lower single scattering albedo (0.81–0.86), reflecting significant absorption in addition to scattering properties. Smoke plumes generate signals in water vapor-sensitive spectral channels due to biomass burning that transports water vapor to the middle and upper troposphere, not because of any inherent spectral similarity. Desert dust remains more easily distinguishable from water vapor because of its distinctly different optical signatures at multiple wavelengths. Therefore, aerosol type discrimination depends on algorithm selection and spectral channel utilization, with smoke–water vapor separation requiring more sophisticated multispectral techniques than dust–water vapor separation.

Currently, there is no vapor correction in Equation (1). The sole correction lies in the careful choice of the clear day. This explains the slight overshoot with the values measured by AERONET, where the AOD is reduced by the vapor contribution. The water vapor column is available among the Sentinel-3 products. The selection of clear day is done without the aid of AERONET, verifying below-threshold values (0.03) of the Sentinel-2 AOD product at 550 nm and simultaneously low water vapor content. In this sense, an asset of DBB-2, with respect to the former DBB [15], is that it is completely unconstrained to the availability of an AERONET station at the test site. The simplest and most straightforward solution is to infer the decrement in the extinction exponent due to the measured column of water vapor, available for S2/3 observations. The correction is then applied to the measured DBB-2. However, the index is no longer automatic. A better solution would be to redesign the index anew. But the more products you use, the easier it is that some will not be available.

Some considerations regarding space–time fusion are in order. The radiometric accuracy of the maps produced by S2 and S3 OLCI is completely comparable. Spatial texture, perhaps partly due to the imperfect cancellation of surface reflectance, is present in the S2 map but not in the OLCI one. Indeed, surface reflectances may have changed between the day of the event and the clear day, as clearly shown for the smoke event, or worse, the BOA reflectance estimate is influenced by atmospheric aerosol content or terrain topography, as in the case of the desert dust event. In the reported tests, the advantage of fusion is minimal, in the sense that OLCI can be used directly on days when S2 is not available. However, in the case of dust or smoke plumes, the advantages of space–time fusion would be immediate [43].

We recognize certain areas for potential methodological improvement. Currently, the index is ineffective on water pixels, such as seas, oceans, lakes, and pools. Adjusting the band selection for the composite index, defining a dedicated water pixel index similar to MODIS's aerosol products, or employing a multiscale approach with Sentinel-3 Sea and Land Surface Temperature Radiometer (SLSTR), which includes thermal bands (albeit at a lower resolution of 500–1000 m), could mitigate this limitation, as aerosol map resolution is not beneficial over water. Despite Sentinel-2's five-day revisit interval, which may miss fast-changing aerosol events, its data remains valuable. There are chances to integrate this with different satellite or ground-based data to achieve a thorough analysis. The spectral range of Sentinel-2 MSI provides extensive detection potential; the lack of thermal infrared bands could inspire complementary approaches. Using a clear-sky baseline for comparisons establishes a robust reference point that, after accurate calibration, can enhance accuracy in future research.

4. Conclusions

This paper introduces a novel methodology for the detection and assessment of aerosols by multispectral (MS) imagery, with a particular emphasis on urban areas within the Mediterranean region. The authors recently proposed a new composite index, dust/biomass burning (DBB), to qualitatively evaluate the presence and concentration of these aerosols [15]. Their prior research adopted data from the Sentinel-2 satellite constellation, which provides high-resolution MS images every five days, complemented by ground-based Aerosol Robotic Network (AERONET) observations, to substantiate their results. A crucial advantage of this index is its robustness against underlying texture variations, which often complicate high-resolution MS satellite products, such as the Sentinel-2 AOD maps in urban settings. The innovation relies on the joint use of Sentinel-2 and Sentinel-3 data to increase the temporal repetition of the AOD observations through a process of fusion of the respective maps. As a further asset of the proposed method, the selection of the clear day, crucial for quantifying the contribution of Rayleigh scattering from atmospheric constituents, is made directly on Sentinel-2 data, without requiring the availability of an AERONET station at the test site.

Experiments have been conducted at a testing site near Potenza, Italy, selected due to its distinct properties and significance in dust aerosol research [42]. A comparison of the values of the DBB-2 index calculated from the MS bands captured during recognized aerosol events with those from clear-sky reference images has been performed. This study demonstrates the ability of the index to discriminate between dust outbreaks and biomass burning events. The matching of DBB values with SDA total AOD measurements, performed by AERONET stations, achieves a 96% accuracy, despite the fact that the average value of the index on land is taken rather than the pixel value at the location of the ground station. A smoke experiment was conducted on datasets from the city of Barcelona, Spain. In this case, the choice of clear day proved critical because of the similar absorption properties of water vapor and smoke. Nevertheless, the average accuracy of the experimental results compared to the AERONET measurements is 95%.

The study demonstrates how DBB-2 is capable of distinguishing between aerosol types, with dust events represented by positive values and biomass burning by negative values. This distinction is vital for an in-depth understanding of the yearly variations and impacts of aerosols on air quality, climate, and public health. Powered by visual assessments and spectral analysis, the research results suggest a promising path to advance RS studies in aerosol identification. We have shown that the merging of DBB-2 maps calculated from S2 or S3 is feasible. The method presented here allows for this, thanks to the definition of overlapped bands in the two satellite instruments, MSI and OLCI. Alternatively, only S2 maps can be calculated every 5 days (cloud permitting) or S3 OLCI maps, which are available every 2 days in regions near the tropics and daily in northern regions, depending on the length of the parallels. Whether merging is useful depends on the presence of smoke or dust plumes. If you need to find images with smoke or dust plumes and an AERONET station within them, the search could become very complicated.

Enhancing the analysis of biomass burning events is possible through the utilization of Sentinel-3 SLSTR's thermal bands, which highlight smoke absorption leading to temperature increases. SLSTR's advantage lies in its daily pass capability as a result of its broader swath compared to that of OLCI. The water vapor band (Oa20) at 940 nm can correct the index values for the scattering of water vapor. Combining Sentinel-2 fine resolution and Sentinel-3 daily data yields frequent and detailed urban aerosol maps validated by AERONET, for efficient dust and smoke detection. However, accuracy declines over water bodies and the lack of thermal bands limits water vapor and smoke corrections. Despite limitations, fusion facilitates operational high-resolution aerosol monitoring with frequent updates and offers a versatile base for further satellite- or ground-based data integration.

Author Contributions: Conceptualization and methodology: L.A., A.G. and S.L.; Validation and software: L.A., M.B. and A.G.; Data curation: M.B. and A.G.; Writing: L.A. and S.L. All authors have read and agreed to the published version of the manuscript.

Funding: This research received no external funding.

Data Availability Statement: The image data can be found here: https://browser.dataspace.copernicus.eu (accessed on 20 October 2025). AERONET data are accessible from https://aeronet.gsfc.nasa.gov/ (accessed on 20 October 2025).

Acknowledgments: The authors thank the AERONET principal investigators and site managers, specifically Lucia Mona and her staff for establishing and maintaining the Tito Scalo (PZ) site, and Alejandro Rodríguez-Gómez and his staff for the Barcelona site, as well as the entire AERONET team for data processing and availability.

Conflicts of Interest: The authors declare no conflicts of interest.

References

1. Baltensperger, U.; Prévôt, A. Chemical analysis of atmospheric aerosols. *Anal. Bioanal. Chem.* **2008**, *390*, 277–280. [CrossRef]
2. Milroy, C.; Martucci, G.; Lolli, S.; Loaec, S.; Sauvage, L.; Xueref-Remy, I.; Lavrič, J.; Ciais, P.; Feist, D.; Biavati, G.; et al. An assessment of pseudo-operational ground-based light detection and ranging sensors to determine the boundary-layer structure in the coastal atmosphere. *Adv. Meteorol.* **2012**, *2012*, 929080. [CrossRef]
3. Zhu, S.; Tang, J.; Zhou, X.; Li, P.; Liu, Z.; Zhang, C.; Zou, Z.; Li, T.; Peng, C. Research progress, challenges, and prospects of PM2.5 concentration estimation using satellite data. *Environ. Rev.* **2023**, *31*, 605–631. [CrossRef]
4. Rosenfeld, D.; Lohmann, U.; Raga, G.; O'Dowd, C.; Kulmala, M.; Fuzzi, S.; Reissell, A.; Andreae, M. Flood or drought: How do aerosols affect precipitation? *Science* **2008**, *321*, 1309–1313. [CrossRef] [PubMed]
5. Gil-Díaz, C.; Sicard, M.; Nabat, P.; Mallet, M.; Muñoz-Porcar, C.; Comerón, A.; Rodríguez-Gómez, A.; Dos Santos Oliveira, D.C.F. Dust aerosol radiative effects during a dust event and heatwave in summer 2019 simulated with a regional climate atmospheric model over the Iberian peninsula. *Remote Sens.* **2025**, *17*, 1817. [CrossRef]
6. Banerjee, T.; Kumar, M.; Singh, N. Aerosol, climate, and sustainability. In *Encyclopedia of the Anthropocene*; Elsevier: Oxford, UK , 2018; Volume 2, pp. 419–428. [CrossRef]
7. Landi, T.C.; Bonasoni, P.; Brunetti, M.; Campbell, J.R.; Marquis, J.W.; Di Girolamo, P.; Lolli, S. Aerosol direct radiative effects under cloud-free conditions over highly-polluted areas in Europe and Mediterranean: A ten-years analysis (2007–2016). *Remote Sens.* **2021**, *13*, 2933. [CrossRef]
8. Bilal, M.; Nichol, J.; Nazeer, M.; Shi, Y.; Wang, L.; Kumar, K.; Ho, H.C.; Mazhar, U.; Bleiweiss, M.; Qiu, Z.; et al. Characteristics of fine particulate matter (PM2.5) over urban, suburban, and rural areas of Hong Kong. *Atmosphere* **2019**, *10*, 496. [CrossRef]
9. Lewis, S.C.; King, A.D.; Perkins-Kirkpatrick, S.E.; Mitchell, D.M. Regional hotspots of temperature extremes under 1.5 °C and 2 °C of global mean warming. *Weather Clim. Extrem.* **2019**, *26*, 100233. [CrossRef]
10. Spiegl, T.; Langematz, U. Twenty-first-century climate change hot spots in the light of a weakening sun. *J. Clim.* **2020**, *33*, 3431–3447. [CrossRef]
11. Lolli, S.; Khor, W.Y.; Matjafri, M.Z.; Lim, H.S. Monsoon season quantitative assessment of biomass burning clear-sky aerosol radiative effect at surface by ground-based Lidar observations in Pulau Pinang, Malaysia in 2014. *Remote Sens.* **2019**, *11*, 2660. [CrossRef]
12. Nakata, M.; Mukai, S.; Fujito, T. Direct detection of severe biomass burning aerosols from satellite data. *Atmosphere* **2022**, *13*, 1913. [CrossRef]
13. Knopp, L.; Wieland, M.; Rättich, M.; Martinis, S. A deep learning approach for burned area segmentation with Sentinel-2 data. *Remote Sens.* **2020**, *12*, 2422. [CrossRef]
14. Apte, J.S.; Manchanda, C. High-resolution urban air pollution mapping. *Science* **2024**, *385*, 380–385. [CrossRef] [PubMed]
15. Lolli, S.; Alparone, L.; Arienzo, A.; Garzelli, A. Characterizing dust and biomass burning events from Sentinel-2 imagery. *Atmosphere* **2024**, *15*, 672. [CrossRef]
16. Lolli, S. Urban PM2.5 concentration monitoring: A review of recent advances in ground-based, satellite, model, and machine learning integration. *Urban Clim.* **2025**, *63*, 102566. [CrossRef]

https://doi.org/10.3390/rs18010116

17. Fan, W.; Qin, K.; Xu, J.; Yuan, L.; Li, D.; Jin, Z.; Zhang, K. Aerosol vertical distribution and sources estimation at a site of the Yangtze River Delta region of China. *Atmos. Res.* **2019**, *217*, 128–136. [CrossRef]
18. Qin, K.; He, Q.; Zhang, Y.; Cohen, J.B.; Tiwari, P.; Lolli, S. Aloft transport of haze aerosols to Xuzhou, Eastern China: Optical properties, sources, type, and components. *Remote Sens.* **2022**, *14*, 1589. [CrossRef]
19. Lolli, S.; Sicard, M.; Amato, F.; Comeron, A.; Gíl-Diaz, C.; Landi, T.C.; Munoz-Porcar, C.; Oliveira, D.; Dios Otin, F.; Rocadenbosch, F.; et al. Climatological assessment of the vertically resolved optical and microphysical aerosol properties by Lidar measurements, sun photometer, and in situ observations over 17 years at Universitat Politècnica de Catalunya (UPC) Barcelona. *Atmos. Chem. Phys.* **2023**, *23*, 12887–12906. [CrossRef]
20. Qu, J.J.; Hao, X.; Kafatos, M.; Wang, L. Asian dust storm monitoring combining Terra and Aqua MODIS SRB measurements. *IEEE Geosci. Remote Sens. Lett.* **2006**, *3*, 484–486. [CrossRef]
21. Dos Santos Oliveira, D.C.F.; Sicard, M.; Rodríguez-Gómez, A.; Comerón, A.; Muñoz-Porcar, C.; Gil-Díaz, C.; Dubovik, O.; Derimian, Y.; Momoi, M.; Lopatin, A. Aerosol forcing from ground-based synergies over a decade in Barcelona, Spain. *Remote Sens.* **2025**, *17*, 1439. [CrossRef]
22. Osborne, M.; Malavelle, F.; Adam, M.; Buxmann, J.; Sugier, J.; Marenco, F.; Haywood, J. Saharan dust and biomass burning aerosols during ex-hurricane Ophelia: observations from the new UK Lidar and sun-photometer network. *Atmos. Chem. Phys.* **2019**, *19*, 3557–3578. [CrossRef]
23. Yang, F.; Fan, M.; Tao, J. An improved method for retrieving Aerosol Optical Depth using Gaofen-1 WFV camera data. *Remote Sens.* **2021**, *13*, 280. [CrossRef]
24. Evgenieva, T.S.; Gurdev, L.; Toncheva, E.; Dreischuh, T. Aerosol types identification during different aerosol events over Sofia, Bulgaria, using sun-photometer and satellite data on the aerosol optical depth and Ångström exponent. *J. Phys. Conf. Ser.* **2022**, *2240*, 012027. [CrossRef]
25. Samulenkov, D.A.; Sapunov, M.V. The aerosol pollution of the atmosphere on the example of Lidar sensing data in St. Petersburg (Russia), Kuopio (Finland), Minsk (Belarus). *Geogr. Environ. Sustain.* **2023**, *16*, 156–163. [CrossRef]
26. Vivone, G.; Arienzo, A.; Bilal, M.; Garzelli, A.; Pappalardo, G.; Lolli, S. A dark target Kalman filter algorithm for aerosol property retrievals in urban environment using multispectral images. *Urban Clim.* **2022**, *43*, 101135. [CrossRef]
27. Ustin, S.L.; Middleton, E.M. Current and near-term advances in Earth observation for ecological applications. *Ecol. Process.* **2021**, *10*, 1. [CrossRef]
28. Alparone, L.; Aiazzi, B.; Baronti, S.; Garzelli, A. *Remote Sensing Image Fusion*; CRC Press: Boca Raton, FL, USA, 2015.
29. Alparone, L.; Arienzo, A.; Garzelli, A. Spatial resolution enhancement of satellite hyperspectral data via nested hypersharpening with Sentinel-2 multispectral data. *IEEE J. Sel. Topics Appl. Earth Observ. Remote Sens.* **2024**, *17*, 10956–10966. [CrossRef]
30. Main-Knorn, M.; Pflug, B.; Louis, J.; Debaecker, V.; Müller-Wilm, U.; Gascon, F. Sen2Cor for Sentinel-2. In *Image and Signal Processing for Remote Sensing XXIII*; Bruzzone, L., Ed.; SPIE: Bellingham, WA, USA, 2017; Proceedings of SPIE; Volume 10427, p. 1042704. [CrossRef]
31. Pacifici, F.; Longbotham, N.; Emery, W.J. The importance of physical quantities for the analysis of multitemporal and multiangular optical very high spatial resolution images. *IEEE Trans. Geosci. Remote Sens.* **2014**, *52*, 6241–6256. [CrossRef]
32. Holben, B.N.; Eck, T.F.; Slutsker, I.; Tanre, D.; Buis, J.P.; Setzer, A.; Vermote, E.; Reagan, J.A.; Kaufman, Y.J.; Nakajima, T.; et al. AERONET—A federated instrument network and data archive for aerosol characterization. *Remote Sens. Environ.* **1998**, *66*, 1–16. [CrossRef]
33. O'Neill, N.; Eck, T.; Smirnov, A.; Holben, B.; Thulasiraman, S. Spectral discrimination of coarse and fine mode optical depth. *J. Geophys. Res. Atmos.* **2003**, *108*, AAC 8-1–AAC 8-15. [CrossRef]
34. Arola, A.; Eck, T.; Kokkola, H.; Pitkänen, M.; Romakkaniemi, S. Assessment of cloud related fine mode AOD enhancements based on AERONET SDA product. *Atmos. Chem. Phys.* **2014**, *17*, 5991–6001. [CrossRef]
35. Torres, B.; Dubovik, O.; Fuertes, D.; Schuster, G.; Cachorro, V.; Lapyonok, T.; Goloub, P.; Blarel, L.; Barreto, A.; Mallet, M.; et al. Advanced characterisation of aerosol size properties from measurements of spectral optical depth using the GRASP algorithm. *Atmos. Measur. Tech.* **2016**, *10*, 3743–3781. [CrossRef]
36. Giles, D.M.; Sinyuk, A.; Sorokin, M.G.; Schafer, J.S.; Smirnov, A.; Slutsker, I.; Eck, T.F.; Holben, B.N.; Lewis, J.R.; Campbell, J.R.; et al. Advancements in the Aerosol Robotic Network (AERONET) Version 3 database–automated near-real-time quality control algorithm with improved cloud screening for Sun photometer aerosol optical depth (AOD) measurements. *Atmos. Measur. Tech.* **2019**, *12*, 169–209. [CrossRef]
37. Li, H.; Jing, L. Improvement of a pansharpening method taking into account haze. *IEEE J. Sel. Topics Appl. Earth Observ. Remote Sens.* **2017**, *10*, 5039–5055. [CrossRef]
38. Lapini, A.; Bianchi, T.; Argenti, F.; Alparone, L. Blind speckle decorrelation for SAR image despeckling. *IEEE Trans. Geosci. Remote Sens.* **2014**, *52*, 1044–1058. [CrossRef]
39. Alparone, L.; Garzelli, A.; Zoppetti, C. Fusion of VNIR optical and C-band polarimetric SAR satellite data for accurate detection of temporal changes in vegetated areas. *Remote Sens.* **2023**, *15*, 638. [CrossRef]

40. Aiazzi, B.; Alparone, L.; Baronti, S.; Garzelli, A.; Selva, M. Advantages of Laplacian pyramids over "à trous" wavelet transforms for pansharpening of multispectral images. In *Image and Signal Processing for Remote Sensing XVIII*; Bruzzone, L., Ed.; SPIE: Bellingham, WA, USA, 2012; Volume 8537, pp. 12–21. [CrossRef]
41. Alparone, L.; Garzelli, A.; Vivone, G. Spatial consistency for full-scale assessment of pansharpening. In Proceedings of the 2018 IEEE International Geoscience And Remote Sensing Symposium, Valencia, Spain, 22–27 July 2018; pp. 5132–5134. [CrossRef]
42. De Rosa, B.; Mytilinaios, M.; Amodeo, A.; Colangelo, C.; D'Amico, G.; Dema, C.; Gandolfi, I.; Giunta, A.; Gumà-Claramunt, P.; Laurita, T.; et al. Observations of Saharan dust intrusions over Potenza, Southern Italy, during 13 years of Lidar measurements: Seasonal variability of optical properties and radiative impact. *Remote Sens.* **2025**, *17*, 453. [CrossRef]
43. Sicard, M.; Granados-Muñoz, M.; Alados-Arboledas, L.; Barragán, R.; Bedoya-Velásquez, A.; Benavent-Oltra, J.; Bortoli, D.; Comerón, A.; Córdoba-Jabonero, C.; Costa, M.; et al. Ground/space, passive/active remote sensing observations coupled with particle dispersion modelling to understand the inter-continental transport of wildfire smoke plumes. *Remote Sens. Environ.* **2019**, *232*, 111294. [CrossRef]

https://doi.org/10.3390/rs18010116